ADVANCED MATERIALS

Supporting Information

for *Adv. Mater.*, DOI 10.1002/adma.202307151

Dynamic Behavior of Spatially Confined Sn Clusters and Its Application in Highly Efficient Sodium Storage with High Initial Coulombic Efficiency

Haoqing Ma, Ruohan Yu, Wangwang Xu, Lei Zhang, Jinghui Chen, Bomian Zhang, Jiantao Li, Xu Xu, Qinyou An*, Weina Xu, Lu Ma, Kumar Varoon Agrawal and Kangning Zhao**

Supporting Information

Dynamic Behavior of Spatially Confined Sn Clusters and its Application in Highly Efficient Sodium Storage with High Initial Coulombic Efficiency

Haoqing Ma, Ruohan Yu, Wangwang Xu, Lei Zhang, Jinghui Chen, Bomian Zhang, Jiantao Li, Xu Xu, Qinyou An*, Weina Xu, Lu Ma, Kumar Varoon Agrawal, Kangning Zhao**

H. M., R. Y., L. Z., J. C., B. Z., J.L., X.X., Q.A.,
State Key Laboratory of Advanced Technology for Materials Synthesis and Processing, Wuhan University of Technology, Wuhan 430070, People's Republic of China
E-mail: zhanglei1990@whut.edu.cn, anqinyou86@whut.edu.cn

H.M., L.Z., J.C., B.Z.
The Sanya Science and Education Innovation Park of Wuhan University of Technology, Sanya 572000, People's Republic of China

W.W.X.
Department of Mechanical Engineering, Louisiana State University Baton Rouge, LA 70803, USA

W.N.X.
School of Material Science and Engineering, Dongguan University of Technology, Dongguan, 523808 China

L.M.
National Synchrotron Light Source II, Brookhaven National Laboratory, Upton, NY, USA

K.V.A., K.Z.
Laboratory of Advanced Separations, École polytechnique fédérale de Lausanne, Sion, 1950, Switzerland
E-mail: kangning.zhao@epfl.ch

Keywords: 3D reconstruction; high initial Coulombic efficiency; interconnected pores; Sn cluster

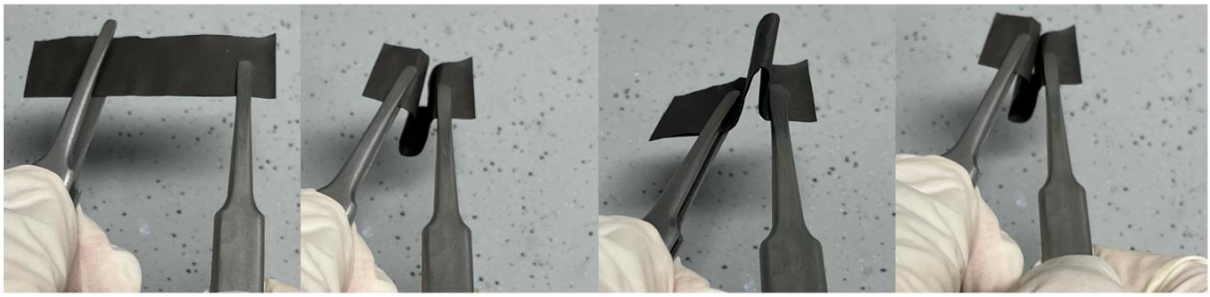

Figure S1. Optical images of Sn–CNF bended back and forth multiple times.

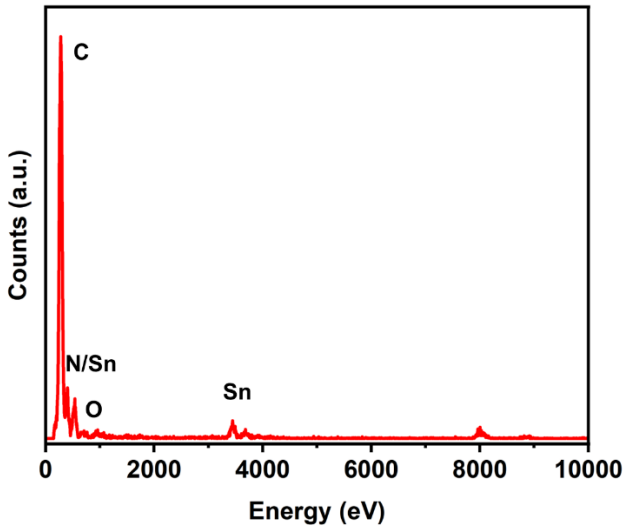

Figure S2. EDS spectra of Sn–CNF for TEM EDS mapping.

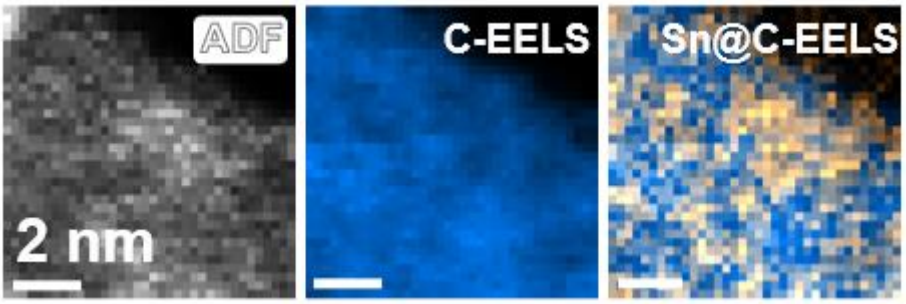

Figure S3. ADF image and EELS mapping of C, Sn, and C mix; Scalebar: 2 nm.

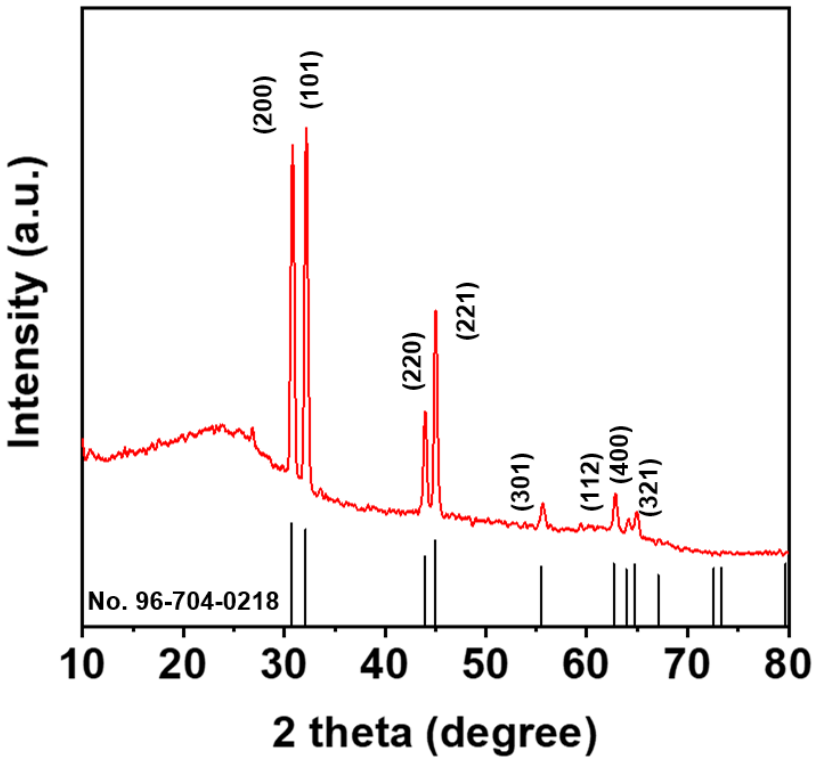

Figure S4. XRD of Sn–CNF.

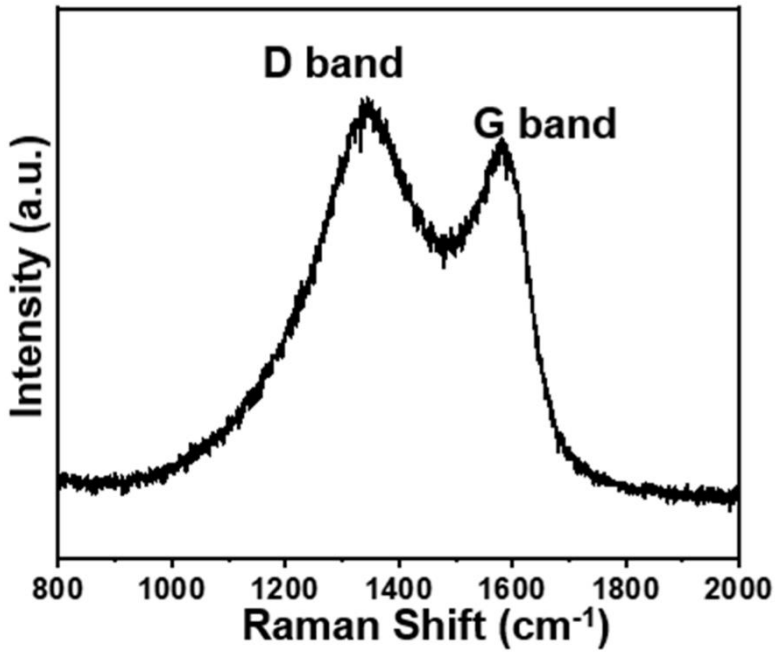

Figure S5. Raman spectrum of Sn–CNF.

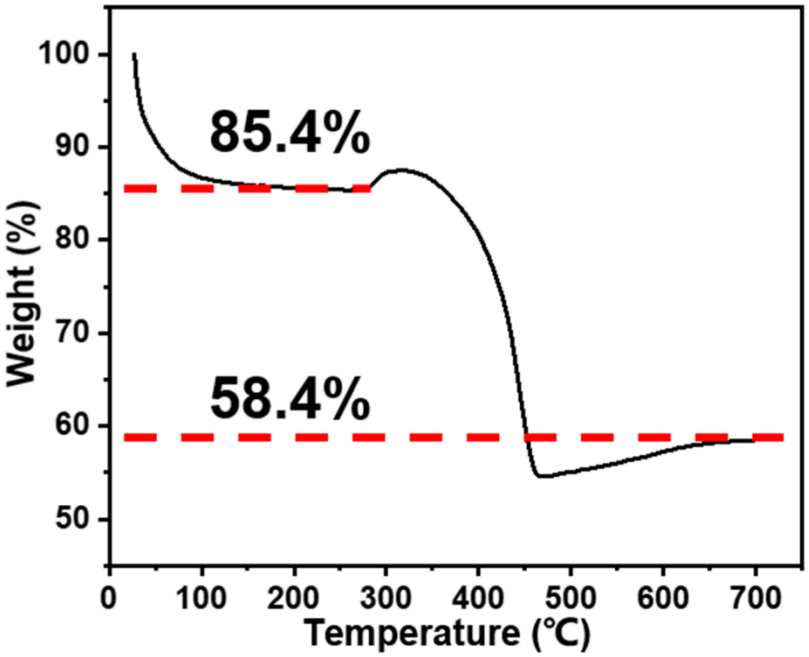

Figure S6. TGA curve of Sn–CNF. TG test is performed in air from room temperature to 700 °C.

Supplementary Note 1. From the TGA curve (Figure S6), ~14.6 % weight loss observed from room temperature to 280 °C was attributed to the evaporation of water absorbed in Sn–CNF. The weight increased with temperature from 280 to 320 °C due to the incomplete oxidation of Sn metal (Sn + O_2 → SnO_x). The quick loss of weight after 320 °C corresponded to the oxidation of C (C + O_2 → CO_2). The increase in weight beyond 450 °C was assigned to the full oxidation of SnO_x (SnO_x + O_2 → SnO_2). The Sn content was calculated using Equation S1[1].

$$Sn\ wt\% = \frac{\frac{58.4\%}{M_{SnO_2}} \times M_{Sn}}{85.4\%} \times 100\% \quad \text{(S1)}$$

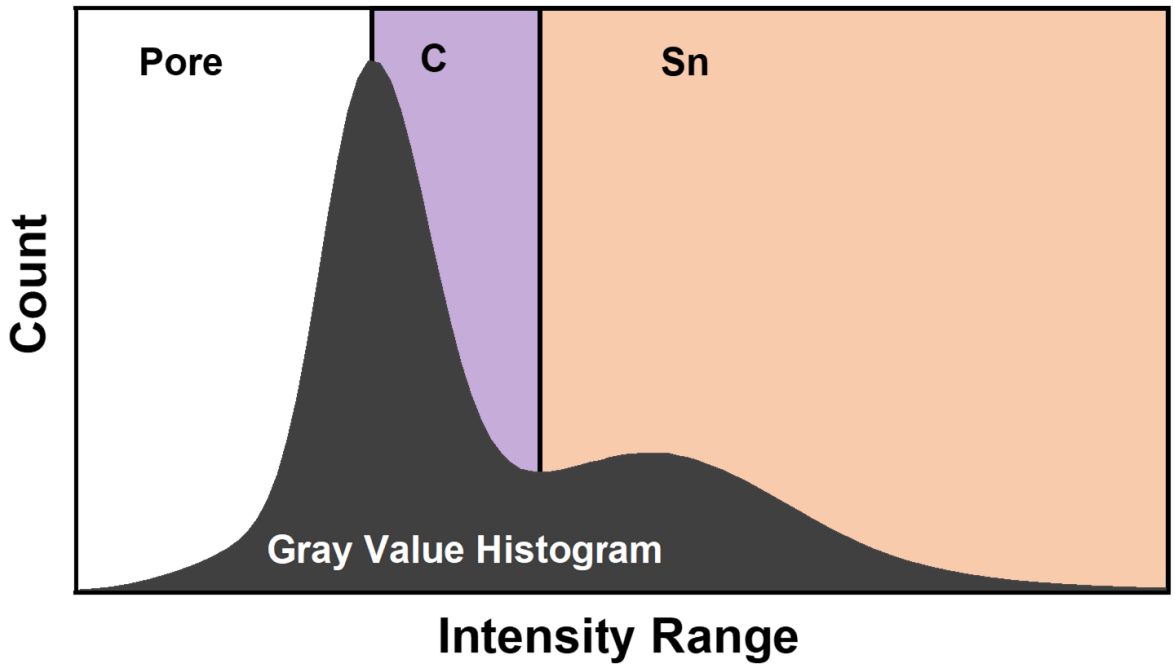

Figure S7. Gray histogram of tomography, the white, purple, and orange regions represent pore, C, and Sn, respectively.

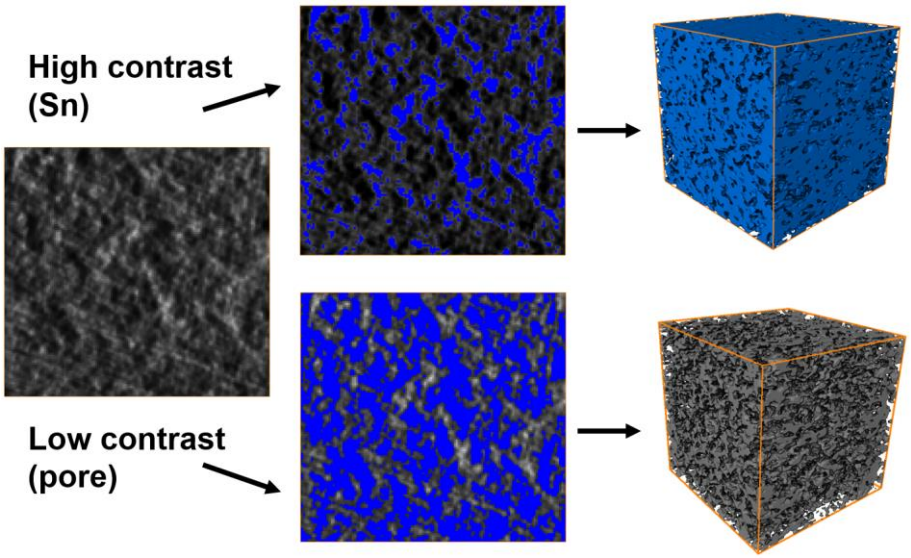

Figure S8. Illustration of segmentation process based on the grey scale from STEM.

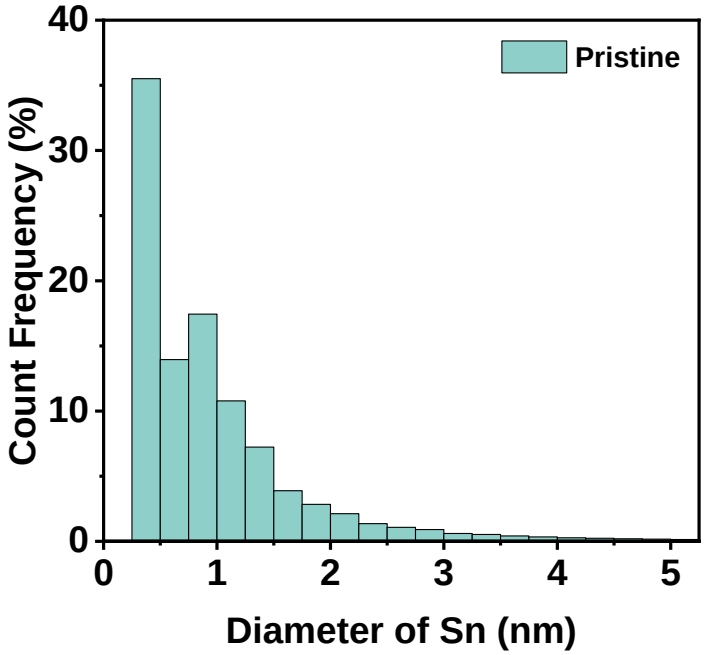

Figure S9. Diameter histogram of Sn from pristine Sn–CNF tomography.

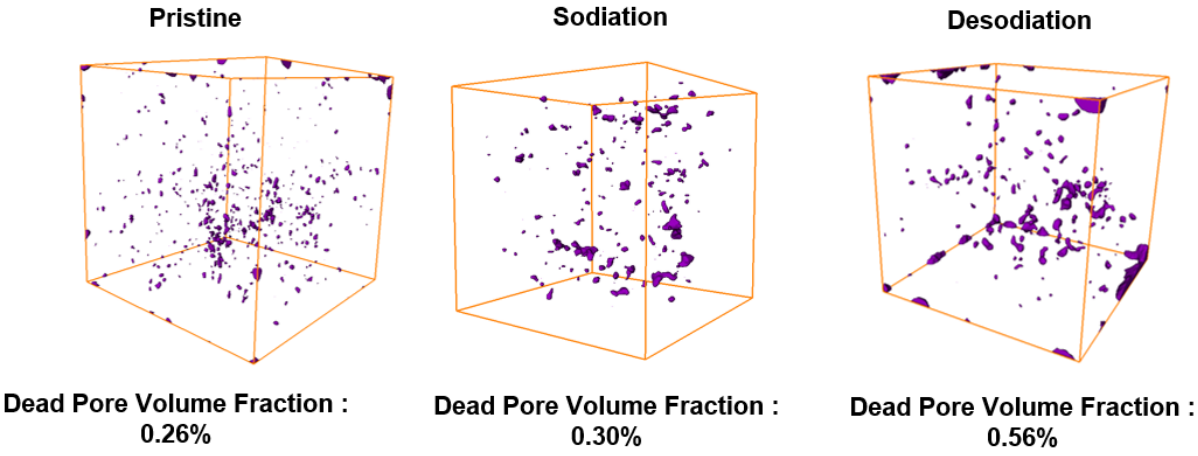

Figure S10. Volume fraction and 3D reconstruction of dead pores from a part of the fiber for pristine, sodiated, and desodiated Sn–CNF.

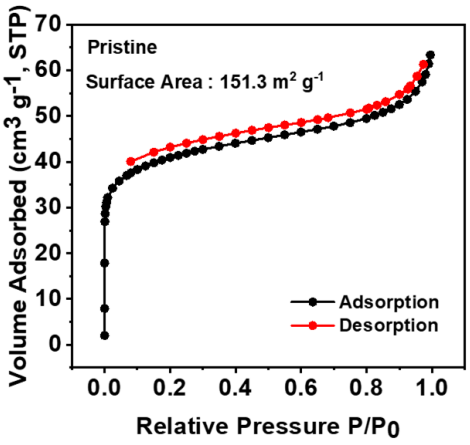

Figure S11. N_2 adsorption–desorption isotherm of Sn–CNF.

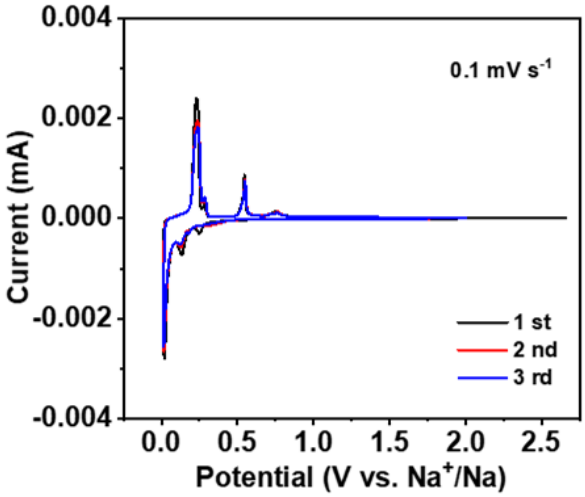

Figure S12. CV curves of Sn–CNF half-cell scanned at a rate of 0.1 mV s^{-1}.

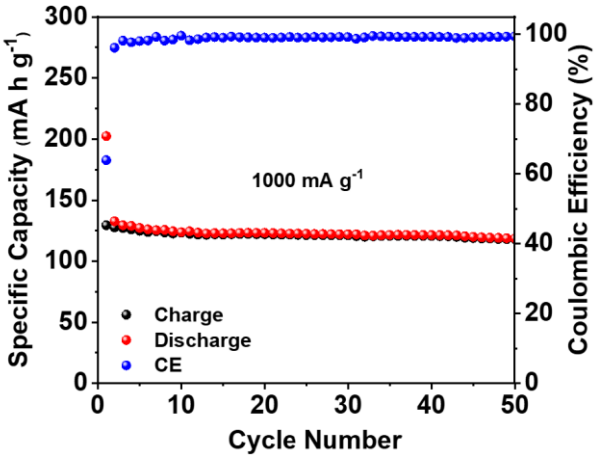

Figure S13. Cycling performance of CNF half-cell at a current density of 1000 mA g^{-1}.

Supplementary Note 2. To evaluate the capacity contribution of CNF, the Sn–CNF mat was immersed in dilute hydrochloric acid for 24 h to remove Sn metal. The capacity of the CNF was tested using a half-cell, which showed a capacity of approximately 120 mAh g^{-1} (Figure S13). Based on the TG test results, the Sn content was 53.9 wt%. The utilization of Sn was calculated using Equation S2 and S3.

$$C_{\mathrm{Sn-CNF}} = C_{\mathrm{Sn}} \times P_{\mathrm{Sn}} + C_{\mathrm{CNF}} \times P_{\mathrm{CNF}} \text{ (S2)}$$

$$Utilization\ of\ Sn = \frac{C_{\mathrm{Sn}}}{C_{\mathrm{Sn\ theoretical}}} \times 100\% \text{ (S3)}$$

where $C_{\mathrm{Sn\text{-}CNF}}$ denotes the capacity of Sn-CNF, C_{Sn} represents the capacity of Sn, C_{CNF} denotes the capacity of CNF, P_{Sn} denotes the weight percentage of Sn, P_{CNF} represents the weight percentage of CNF, and $C_{\mathrm{Sn\ theoretical}}$ denotes the theoretical capacity of Sn.

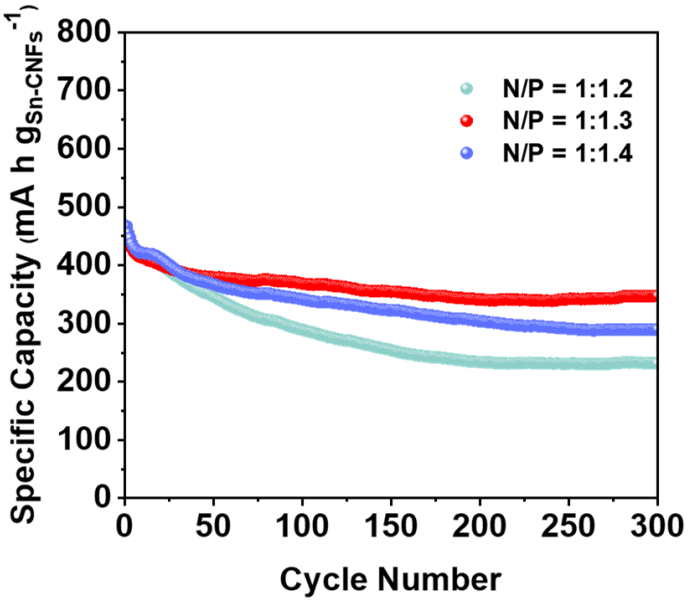

Figure S14. Sn–CNF–NVP full-cell performance with different N/P ratio (based on anode).

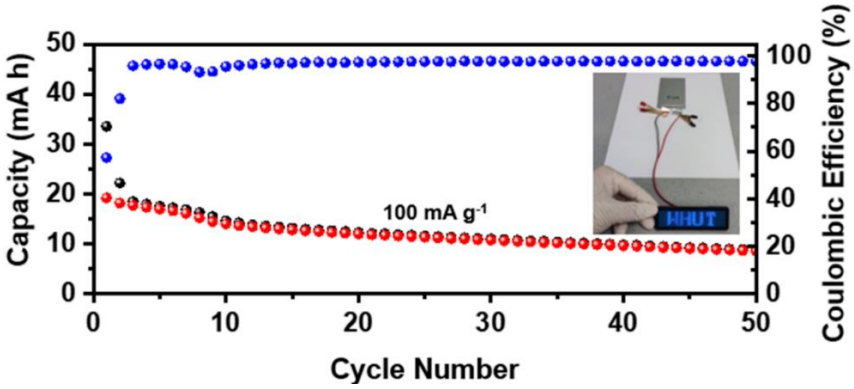

Figure S15. Pouch cell cycling performance of Sn–CNF–NVP; the inset optical image shows a digital image of the lit light-emitting diode.

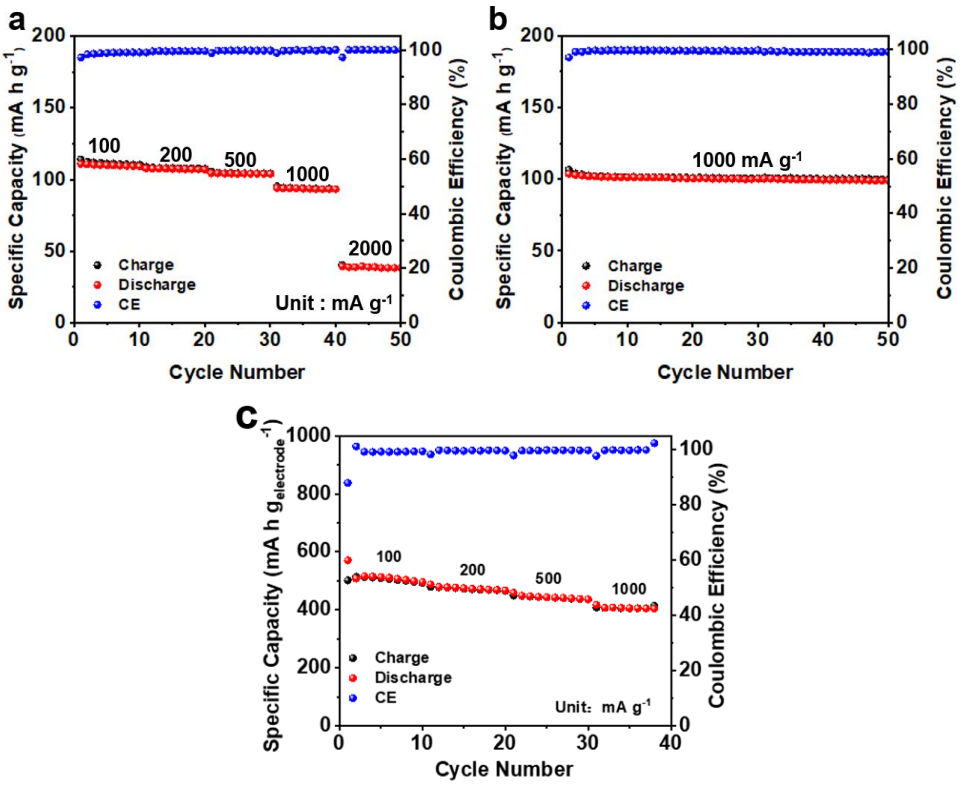

Figure S16. a) Rate capability of NVP half-cell vs Na metal. b) Cycling performance of NVP half-cell at a current density of 1000 mA g^{-1}. c) Rate capability of Sn–CNF half-cell vs Na metal.

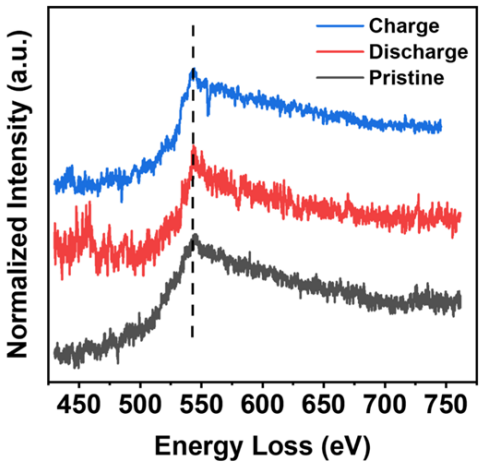

Figure S17. *Ex situ* EELs of Sn-CNF with normalized intensity.

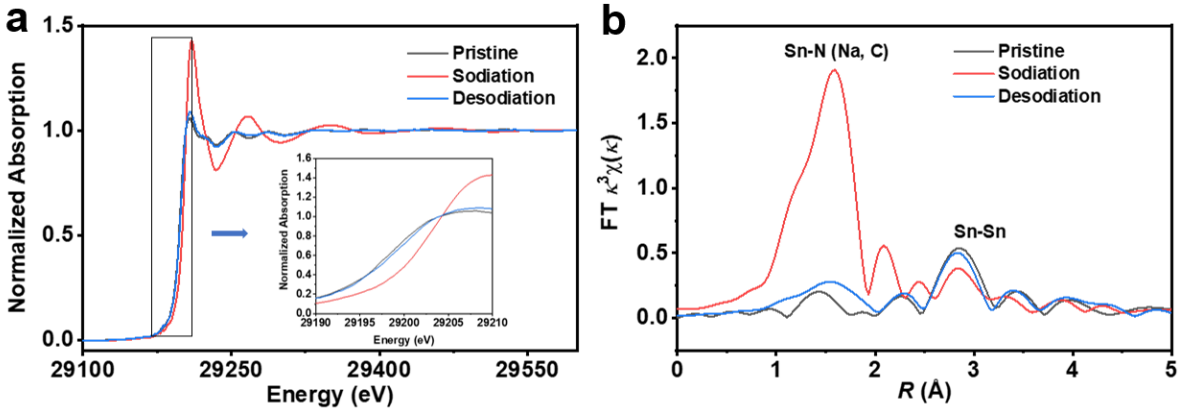

Figure S18. a) *Ex situ* Sn K-edge XANES. b) *Ex situ* Fourier transformation curves of EXAFS for Sn edges.

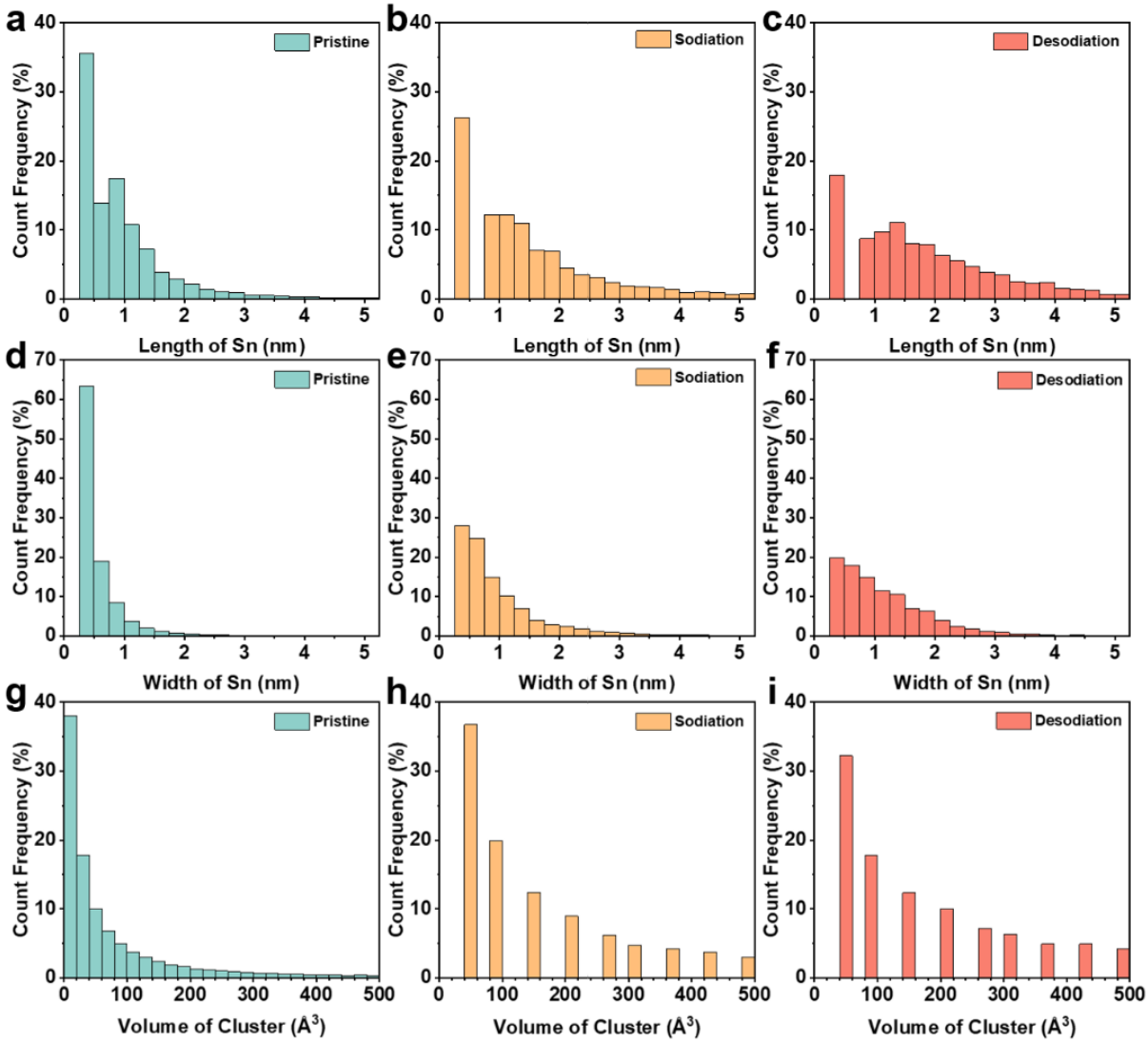

Figure S19. A–c) Length histogram of Sn for pristine, sodiated, and desodiated Sn–CNF. d-f) Width histogram of Sn for pristine, sodiation, and desodiation Sn-CNF. g-i) Volume histogram of Sn for pristine, sodiation, and desodiation Sn-CNF.

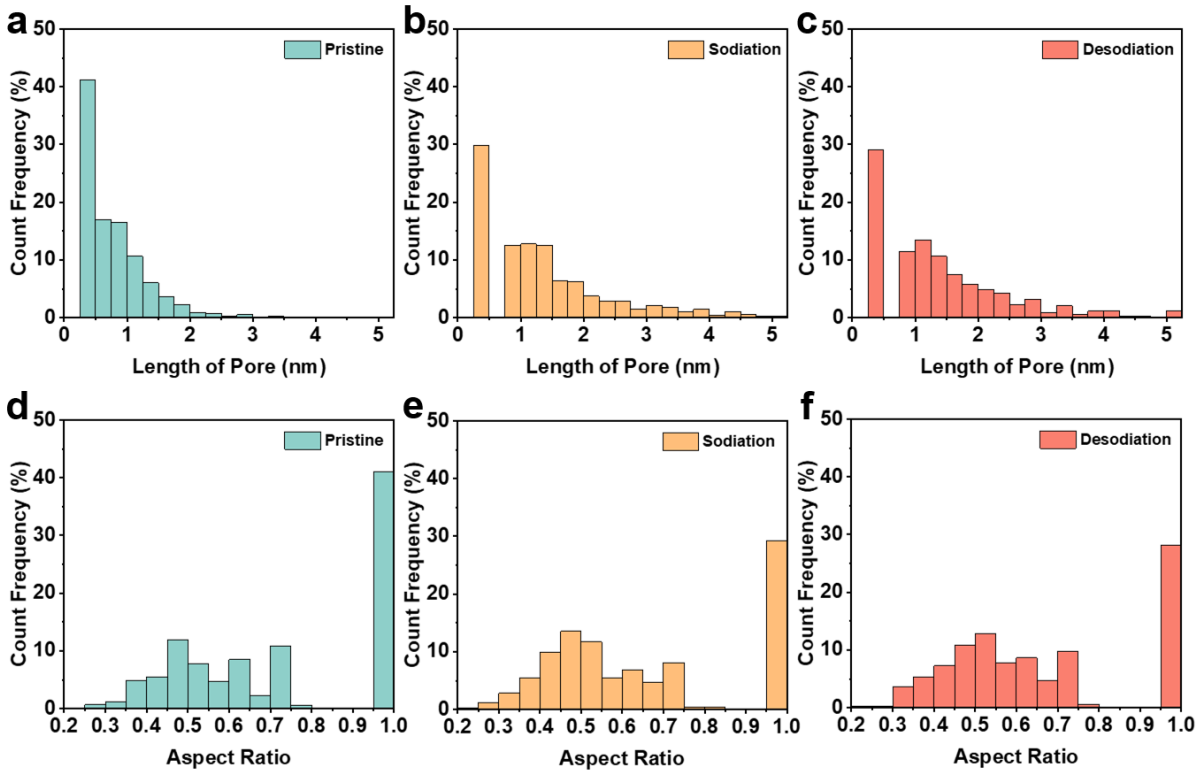

Figure S20. a-c) Length histogram of pore for pristine, sodiation, and desodiation Sn-CNF. d-f) Aspect ratio histogram of pore for pristine, sodiation, and desodiation Sn-CNF.

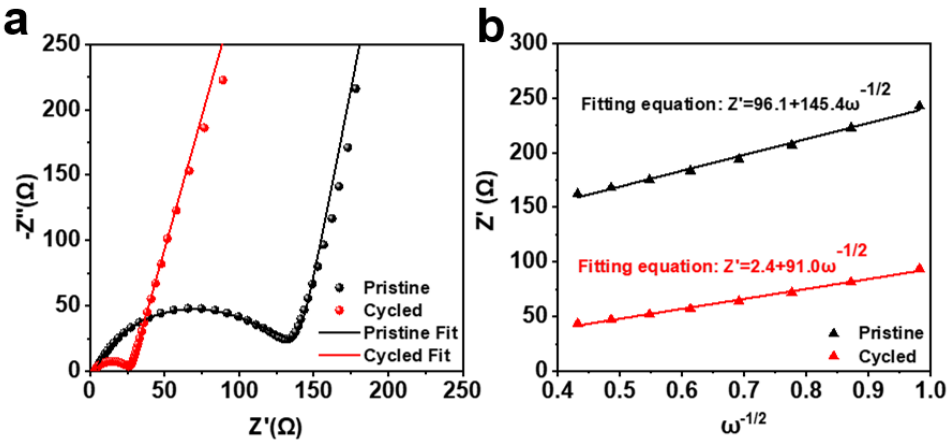

Figure S21. a) Nyquist plots of the Sn-CNF half cells and fit curve. b) Real parts of the impedance (Z') versus the reciprocal square root of the angular frequency ($\omega^{-1/2}$) in the low frequency region of Sn-CNF half cell.

Supplementary Note 3. The Nyquist plot consists of a semicircular curve at high frequencies and a straight line in the low-frequency region. The x-intercept of the plot at high frequency is determined by the solution resistance (noted as R_s), which are respectively 3.86 and 3.16 Ω for pristine and cycled (only cycled once) Sn-CNF half cell, and the end of the semicircle at low

frequency originated from the charge transfer resistance (noted as R_{ct}), which are respectively 120.97 and 19.63 Ω for pristine and cycled (only cycled once) Sn-CNF half cell. It's obvious that the transfer resistance reduced after sodiation and desodiation, the straight line in the low frequency region indicates the Warburg element, and the low frequency region is investigated in Z'-$\omega^{-1/2}$ plot and then calculated with Equation S4 and Equation S5. The value of σ was calculated by Equation S5 and the fitting results of Z'-$\omega^{-1/2}$ plot which is displayed in Figure S21, the σ value of pristine and cycled Sn-CNF is 145.4 and 91.0 respectively, and this result indicates that the diffusion coefficient of Na^+ ions (D_{Na+}) increases with the structure change occurred in the de/sodiation process according to Equation S2[2]. The corresponding equivalent circuits are shown in Figure S22.

$$D_{Na^+} = \frac{R^2T^2}{2A^2n^4F^4C^2\sigma^2} \quad \text{(S4)}$$

$$Z' = R_D + R_L + \sigma\omega^{-1/2} \quad \text{(S5)}$$

Equation S4 and **Equation S5.** Equation to calculate the diffusion coefficient of Na^+ ions (D_{Na+}).

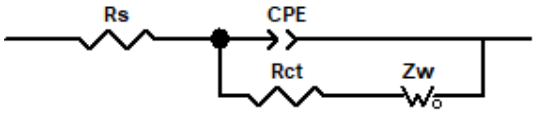

Figure S22. Equivalent circuit of EIS.

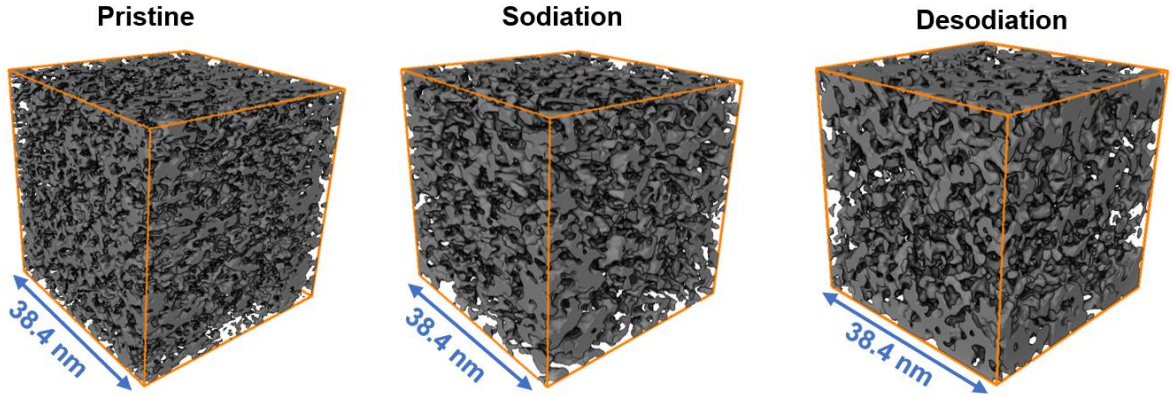

Figure S23. The shape illustration for pore of pristine, sodiated, and desodiated Sn-CNF from tomography (the gray part stands for pore).

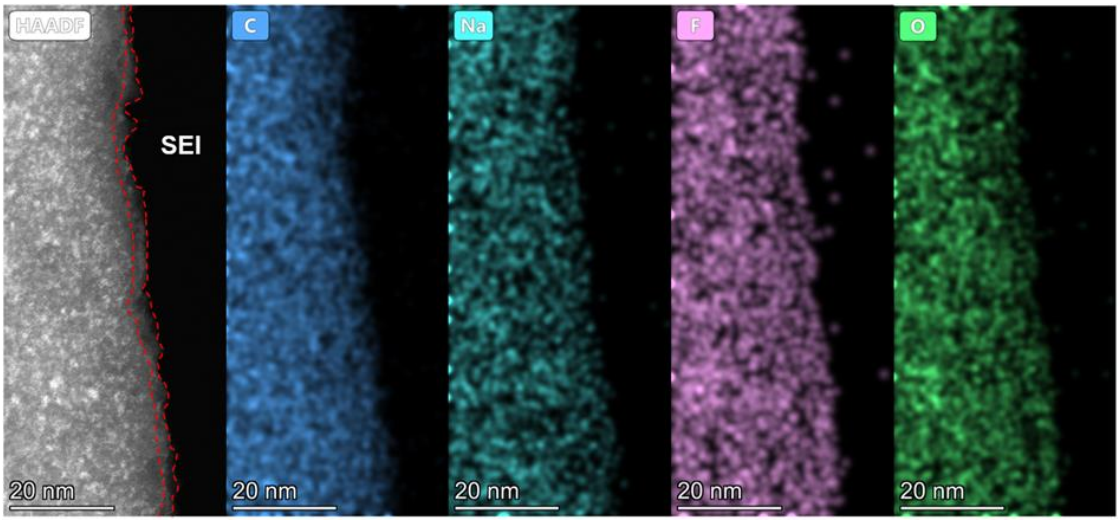

Figure S24. TEM and EDS mapping of C, Na, F, and O from cycled Sn–CNF.

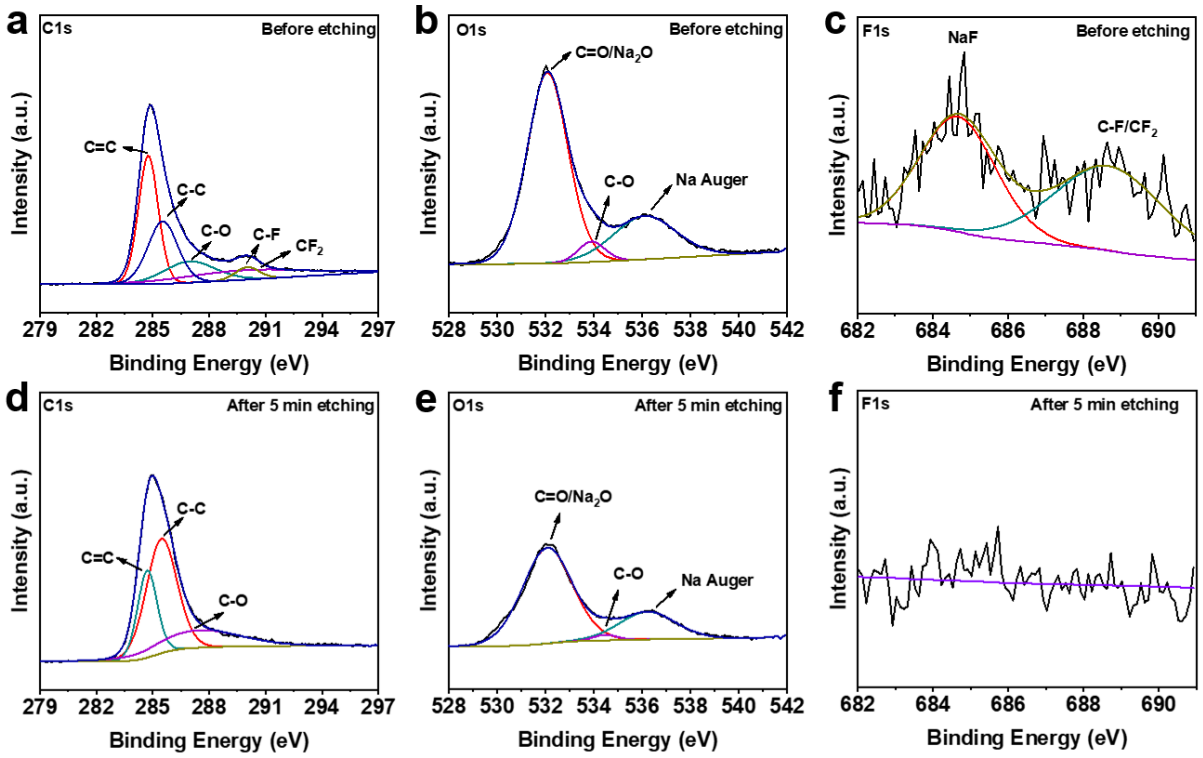

Figure S25. a–c) C1s, O1s, and F1s spectra of cycled Sn–CNF before etching. D–f) C1s, O1s, and F1s spectra of cycled Sn–CNF after 5 min of etching.

Supplementary Note 4. After cycling, the Sn–CNF electrode sheet was washed thrice with DME to remove residual electrolyte for depth profile XPS characterization. The depth profile XPS suggested that after only 5 min, the signals of NaF and -CF_x disappeared, indicating the

ultra-thin nature of the SEI layer. The inorganic part of the SEI layer was composed of NaF and Na_2O.

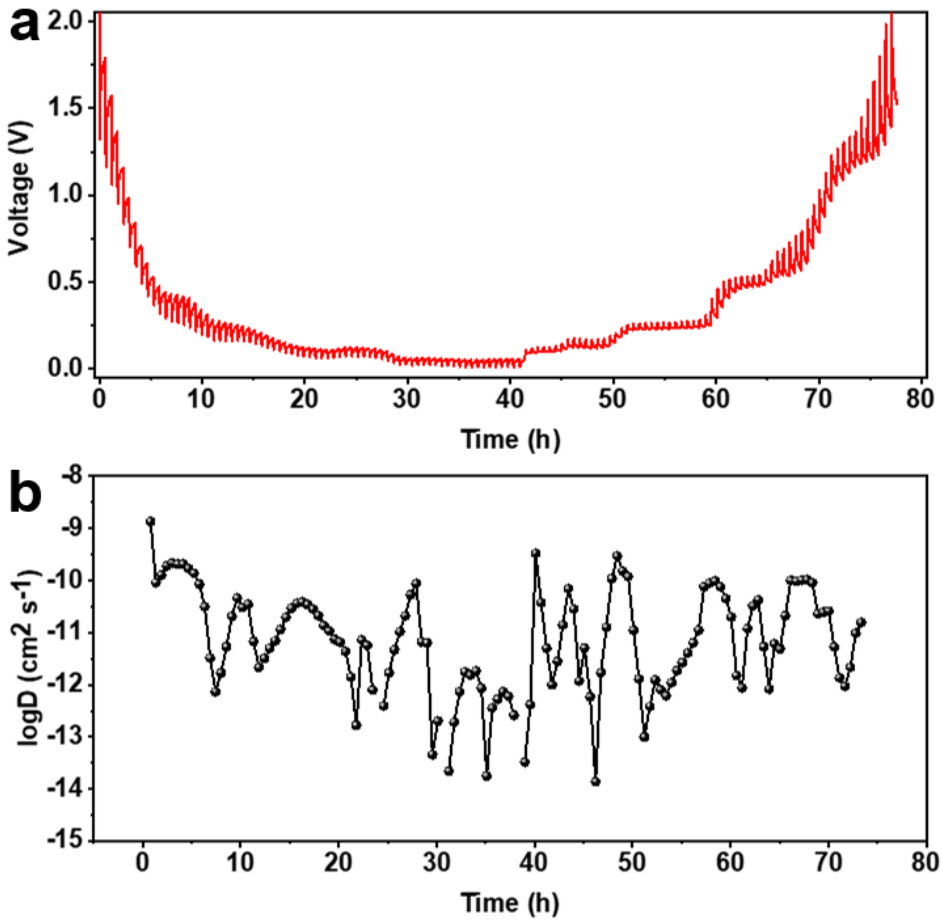

Figure S26. a) GITT time–voltage curve tested at a current density of 100 mA g^{-1} with 5-min pulse and 30-min relax. b) Time-logD curve calculated by GITT.

Table S1. Performance comparison with the state-of-the-art literatures.

Material	Particle Size	ICE	Utilization	Areal capacity	Specific Capacity	Battery Type	Reference
SnS/SnOx hollw nanospheres	15 nm	57%	46%	-	550 mAh g^{-1} at 100 mA g^{-1}	Na	[3]
Sn/$FeSn_2$@C	150 nm	93.80%	75%	-	462.8 mAh g^{-1} at 1000 mA g^{-1}	Na	[4]
SnO_2@PEG-GO	~4 nm	60-70%	51%	2.92 mAh cm^{-2} (Li) 1.01 mAh cm^{-2} (Na)	1523 mAh g^{-1} at 100 mA g^{-1}(Li) 527 mAh g^{-1} at 50 mA g^{-1}(Na)	Li/Na	[5]

Sn/SnO2@C Hollow Nanofibers	~20-30 nm	60-70%	58%	1.97 mAh cm^{-2}	986.3 mAh g^{-1} at 1000 mA g^{-1}	Li	[6]
Tin-graphene tubes	40 nm	71%	60% at 5A g-1	5.4 mAh cm^{-2}	916 mAh g^{-1} at 200 mA g^{-1}	Li	[7]
Sn_2(dobpdc)	single atom	40-50%	92.60%	1.32-1.53 mAh cm^{-2}	1018 mAh g^{-1} at 200 mA g^{-1}	Li	[8]
SnO_2–Mo	a few nm layer deposition	92.60%	-	-	1067 mAh g^{-1} at 200 mA g^{-1}	Li	[9]
Zn-doped hard carbon	-	84%	-	3 mAh cm^{-2} (half cell) 0.45 mAh cm^{-2} (full cell)	402 mAh g^{-1} at 1000 mA g^{-1}	Na	[10]
MgO-Hard carbon	-	88%	-	0.4-0.52 mAh cm^{-2}	400 mAh g^{-1} at 250 mA g^{-1}	Na	[11]
Sulfur-containing carbonaceous	-	~30-40%	-	0.29-0.58 mAh cm^{-2}	290 mAh g^{-1} at 1000 mA g^{-1}	Na	[12]
UPCs	-	71.50%	-	0.34-0.42 mAh cm^{-2}	305 mAh g^{-1} at 1000 mA g^{-1}	Na	[13]
Sn-CNF	0.25-4 nm	87%	95%	2.27 mAh cm^{-2} (half cell) 1.91 mAh cm^{-2} (full cell)	808 mAh g^{-1} at 1000 mA g^{-1}	Na	This work

Reference

[1] Y. Liu, N. Zhang, L. Jiao, Z. Tao, J. Chen, Adv. Funct. Mater. 2015, 25, 214.

[2] a)W. Duan, Z. Zhu, H. Li, Z. Hu, K. Zhang, F. Cheng, J. Chen, J. Mater. Chem. A 2014, 2, 8668; b)X.-L. Wu, Y.-G. Guo, J. Su, J.-W. Xiong, Y.-L. Zhang, L.-J. Wan, Adv. Energy Mater. 2013, 3, 1155.

[3] H. Bian, Z. Li, X. Xiao, P. Schmuki, J. Lu, Y. Y. Li, Adv. Funct. Mater. 2019, 29.

[4] M. Chen, P. Xiao, K. Yang, B. Dong, D. Xu, C. Yan, X. Liu, J. Zai, C. J. Low, X. Qian, Angew. Chem. Int. Ed. 2023, 62, e202219177.

[5] S. Zhao, Y. He, Z. Wang, X. Bo, S. Hao, Y. Yuan, H. Jin, S. Wang, Z. Lin, Adv. Energy Mater. 2022, 12.

[6] S. Gao, N. Wang, S. Li, D. Li, Z. Cui, G. Yue, J. Liu, X. Zhao, L. Jiang, Y. Zhao, Angew. Chem. Int. Ed. 2020, 59, 2465.

[7] R. Mo, X. Tan, F. Li, R. Tao, J. Xu, D. Kong, Z. Wang, B. Xu, X. Wang, C. Wang, J. Li, Y. Peng, Y. Lu, Nat Commun 2020, 11, 1374.

[8] J. Liu, D. Xie, X. Xu, L. Jiang, R. Si, W. Shi, P. Cheng, Nat Commun 2021, 12, 3131.

[9] X. Lan, J. Cui, X. Zhang, R. Hu, L. Tan, J. He, H. Zhang, X. Xiong, X. Yang, S. Wu, M. Zhu, Adv Mater 2022, 34, e2106366.

[10] Z. Lu, J. Wang, W. Feng, X. Yin, X. Feng, S. Zhao, C. Li, R. Wang, Q. A. Huang, Y. Zhao, Adv Mater 2023, e2211461.

[11] A. Kamiyama, K. Kubota, D. Igarashi, Y. Youn, Y. Tateyama, H. Ando, K. Gotoh, S. Komaba, Angew. Chem. Int. Ed. 2021, 60, 5114.

[12] J. Tzadikov, N. R. Levy, L. Abisdris, R. Cohen, M. Weitman, I. Kaminker, A. Goldbourt, Y. Ein‐Eli, M. Shalom, Adv. Funct. Mater. 2020, 30.

[13] J. Yan, H. Li, K. Wang, Q. Jin, C. Lai, R. Wang, S. Cao, J. Han, Z. Zhang, J. Su, K. Jiang, Adv. Energy Mater. 2021, 11.